



## Original paper

## Highly multiplexed SiPM signal readout for brain-dedicated TOF-DOI PET detectors

Haewook Park<sup>a,b</sup>, Jae Sung Lee<sup>a,b,c,d,\*</sup><sup>a</sup> Department of Biomedical Sciences, Seoul National University College of Medicine, Seoul 03080, South Korea<sup>b</sup> Department of Nuclear Medicine, Seoul National University College of Medicine, Seoul 03080, South Korea<sup>c</sup> Institute of Radiation Medicine, Medical Research Center, Seoul National University College of Medicine, Seoul 03080, South Korea<sup>d</sup> Brightonix Imaging Inc., Seoul 04782, South Korea

## ARTICLE INFO

## Keywords:

Positron emission tomography (PET)

Silicon photomultiplier (SiPM)

Multiplexing

Depth-of-interaction (DOI)

Time-of-flight (TOF)

## ABSTRACT

**Purpose:** We investigated the highly multiplexed readout of SiPM signals that are useful in developing brain-dedicated PET detectors with DOI-capable crystal blocks and large-area SiPM arrays.

**Methods:** The PET detector module used in this study was equipped with a two-layer relative-offset DOI crystal block and a  $2 \times 2$  array of 16-channel SiPMs. The lower crystal-layer consisted of a  $14 \times 14$  array of  $1.78 \times 1.78 \times 8$  mm<sup>3</sup> LSO crystals and the upper crystal-layer consisted of a  $13 \times 13$  array of  $1.78 \times 1.78 \times 12$  mm<sup>3</sup> LSO crystals. The energy and position information was obtained via signals from the  $8 \times 8$  resistive charge division multiplexing circuit. The timing performance was evaluated with varying multiplexing ratios (i.e. 16:1, 32:1, and 64:1) via first-order analog high-pass filtering.

**Results:** For three different multiplexing schemes, all LSO crystals with two-layer DOI information were clearly resolved and yielded good energy resolutions of  $10.5 \pm 1.0\%$  (upper) and  $12.1 \pm 1.7\%$  (lower). The 16:1 multiplexing yielded an optimal timing performance with average CRT values of 325 ps FWHM (upper) and 342 ps FWHM (lower); however, the timing performances were maintained almost constant even for 64:1 multiplexing with average CRT values of 336 ps FWHM (upper) and 347 ps FWHM (lower).

**Conclusions:** The highly multiplexed SiPM signal readout via the first-order analog high-pass filtering could be an attractive solution to develop brain-dedicated PET scanners, effectively decreasing the burden of DAQ systems with moderate compromise in terms of TOF and DOI performances.

## 1. Introduction

One of the most actively investigated imaging devices in the recent nuclear medicine society is the brain-dedicated positron emission tomography (PET) scanner with high resolution and high sensitivity [1–8]. Unlike the whole-body PET scanner, the smaller bore size of the brain-dedicated PET scanner enhances the geometric efficiency of photon detection and decreases the positioning error due to non-collinearity in 511-keV photon annihilations. Furthermore, the use of smaller crystal elements in the brain-dedicated PET scanner yields a better spatial resolution than that obtained with the whole-body PET scanner, because the intrinsic resolution of the PET detector is a major limiting factor in determining the spatial resolution of the PET system.

Brain-dedicated PET scanners feature a smaller bore size and smaller crystal elements, thus the severity of the parallax error increases due to photon penetration via the side-surface of crystal

elements and worsens spatial resolution toward the periphery of the PET scanner. The parallax error can be mitigated by measuring the depth-of-interaction (DOI) information. Measurement of DOI provides uniform spatial resolution throughout the PET scanner and also improves the timing resolution of the PET system by compensating the time-walk as a function of DOI positions [9–11]. One of the most popular approaches to determining the DOI position is a relative-offset method in which the multilayer crystal arrays are stacked with half crystal-pitch offsets from other layers [12–14]. The relative-offset DOI method enables a discrete three-dimensional (3D) position decoding of interacted gamma photons from a two-dimensional (2D) flood histogram. The density of crystal elements is almost doubled in the 2D flood histogram via the relative-offset DOI method, thus multilayer crystal arrays are typically coupled to the photosensors with high granularity (e.g. array-type silicon photomultipliers (SiPMs) or multianode position-sensitive photomultiplier tubes (PMTs)) to obtain a clearer

\* Corresponding author at: Department of Nuclear Medicine, Seoul National University College of Medicine, Daehak-ro, 101, Jongno-gu, Seoul 03080, South Korea.  
E-mail address: [jaes@snu.ac.kr](mailto:jaes@snu.ac.kr) (J.S. Lee).

<https://doi.org/10.1016/j.ejmp.2019.11.016>

Received 3 September 2019; Received in revised form 12 November 2019; Accepted 18 November 2019

1120-1797/ © 2019 Published by Elsevier Ltd on behalf of Associazione Italiana di Fisica Medica.

separation of crystal elements from the 2D flood histogram.

It is also important to accurately measure time-of-flight (TOF) information in brain-dedicated PET scanners. The improvement of signal-to-noise ratio (SNR) was not significantly considered for brain PET images obtained from PMT-based whole-body PET scanners with 500-ps level timing resolution (e.g. Siemens *Biograph mCT*, GE *Discovery 690/710*, and Philips *Ingenuity TF*). However, the recent advances in PET timing performance based on state-of-the-art SiPM technologies have allowed the brain to function as an organ that takes great benefits from the TOF information [15–17]. Deep learning approaches are also actively investigated in various medical imaging fields [18–21]. With respect to brain PET imaging, for example, the attenuation and scatter correction of the brain PET images based on simultaneous activity and attenuation reconstruction algorithms augmented by TOF information and deep learning approaches have further improved the quantitative accuracy of brain-dedicated PET scanners without computed tomography (CT) machine [22,23].

With respect to the development of SiPM-based brain-dedicated PET systems, a large number of readout channels are generally required due to the high-granularity of SiPM arrays and crystal elements. Therefore, reducing the number of SiPM signals at early analog front-end stages corresponds to a practical solution to decrease the readout burdens of subsequent data acquisition (DAQ) systems [24–27]. One dominant factor that affects the timing resolution in SiPM-based PET scanners is the multiplexing ratio of SiPM signals. This is because the timing performance of the PET system worsens as the multiplexing ratio increases [28].

One practical method to mitigate the timing degradation while multiplexing SiPM signals involves the use of an analog filtering method. Previous studies by Bienosek *et al.* [29,30] suggested a simple capacitive coupling technique that only requires a small number of passive electronic components. This approach effectively decreases the baseline fluctuation of highly multiplexed SiPM signals via preventing a pileup of continuous dark currents of SiPM arrays. However, their investigations were limited to PET detectors with a 16-channel SiPM array that was one-to-one coupled with 3-mm-pitch crystal elements, and the multiplexing ratio was also limited to 16:1.

Therefore, in this study, we further investigated and characterized the highly multiplexed SiPM readout scheme via a high-resolution PET detector module with a DOI-capable crystal block and large-area SiPM array. Specifically, we investigated timing characteristics of the PET detector module with variations in the multiplexing ratio of a 64-channel SiPM array (i.e. 16:1, 32:1, and 64:1) via first-order high-pass filtering. We expect that the highly multiplexed SiPM signal readout via the first-order high-pass filter could be a simple and practical solution to develop brain-dedicated PET scanners, thereby effectively decreasing data volumes in subsequent DAQ systems with moderate compromises in terms of TOF and DOI performances.

## 2. Materials and methods

### 2.1. PET detector module

The PET detector module investigated in this study is composed of a two-layer relative-offset DOI crystal block (Sichuan Tianle Photonics, China) and four monolithic 16-channel through-silicon-via (TSV) SiPMs (S13361-3050NE-04; Hamamatsu Photonics K.K., Japan) as shown in Fig. 1. The upper crystal-layer consisted of a  $13 \times 13$  array of  $1.78 \times 1.78 \times 8 \text{ mm}^3$  lutetium oxyorthosilicate (LSO) crystals and the lower crystal-layer consisted of a  $14 \times 14$  array of  $1.78 \times 1.78 \times 12 \text{ mm}^3$  LSO crystals. All the LSO crystals were polished and optically isolated with an enhanced spectral reflector (ESR; 3 M, US). The four monolithic 16-channel SiPMs with identical breakdown voltages were assembled into a  $2 \times 2$  array and mounted on the top layer of a printed circuit board (PCB). Each of the 64 SiPM outputs was routed into a 100-pin ultra-fine pitch socket (ST4-50-1.00-LNP-D-P-TR;

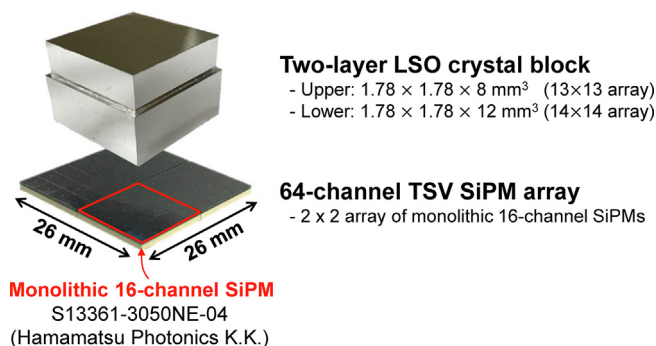


Fig. 1. PET detector module used in this study.

SAMTEC, Singapore) such that all the SiPM signals were extracted from the bottom layer of the PCB. The LSO crystal block and 64-channel SiPM array were coupled via optical grease (BC-630; Saint-Gobain, France).

### 2.2. Front-end electronics

Figs. 2 and 3 illustrate detailed schematics of front-end electronics for processing analog output signals from the 64-channel SiPM array. A position encoding network was implemented based on a  $8 \times 8$  resistive discretized positioning circuit (DPC) [31] as shown in Fig. 2. The resistive DPC generates four corner-node signals. Each of the corner-node signals was fed into a non-inverting low-gain amplifier (AD8000; Analog Devices, US) with an input impedance ( $R_{\text{input}}$ ) corresponding to  $47 \Omega$ . Subsequently, the amplified corner-node signals (i.e. *Position signals*; A, B, C, and D) were used to obtain position and energy information of the PET detector module. With respect to timing information, three different multiplexing readouts of the 64-channel SiPM array were implemented as described in Fig. 3. With respect to 16:1 multiplexing, the 16 anodes from each of single monolithic 16-channel SiPMs were reduced into four timing outputs. With respect to 32:1 multiplexing, the 32 anodes from two monolithic 16-channel SiPMs were reduced into two timing outputs. With respect to 64:1 multiplexing, the 64 anodes from four monolithic 16-channel SiPMs were reduced into a single timing output. The multiplexed SiPM anodes were amplified via a non-inverting high-gain amplifier (AD8000; Analog Devices, US) after passing them through a first-order high-pass filter. The first-order high-pass filter was simply implemented via a series capacitor ( $C_{\text{filter}}$ ) and shunt resistor ( $R_{\text{filter}}$ ) at the input terminal of the high-gain amplifier. Specifically, all the lengths of 64 PCB traces towards the high-gain amplifier were identically matched to minimize the delay difference during signal propagation. Each of the multiplexed SiPM anodes was then divided into two routes following signal amplification, wherein one route functioned as an input for waveform sampling (i.e. *Timing signals*;  $T_1$ ,  $T_2$ ,  $T_3$ , and  $T_4$ ) to obtain timing information and the other route functioned as an input for an LVCMOS comparator (ADCMP601; Analog Devices, US) to generate trigger from the 64-channel SiPM array. The comparator threshold ( $V_{\text{thre}}$ ) was set as 50 mV via a 12-bit digital-to-analog converter (DAC) (AD5629; Analog Devices, US). Subsequently, the comparator output was connected to a digital OR logic gate (SN74AC32; Texas Instruments, US) to generate a *Module trigger* for a subsequent DAQ system.

### 2.3. Experimental setup

Fig. 4 shows the experimental setup used in this study. We used a reference detector based on a Hamamatsu R9800 photomultiplier tube (PMT) and a  $4 \times 4 \times 10 \text{ mm}^3$  single lutetium-yttrium oxyorthosilicate (LYSO) crystal. The single timing resolution (STR) of the reference detector corresponded to 243 ps full-width at half-maximum (FWHM). The PET detector module was located 20-cm away from the reference

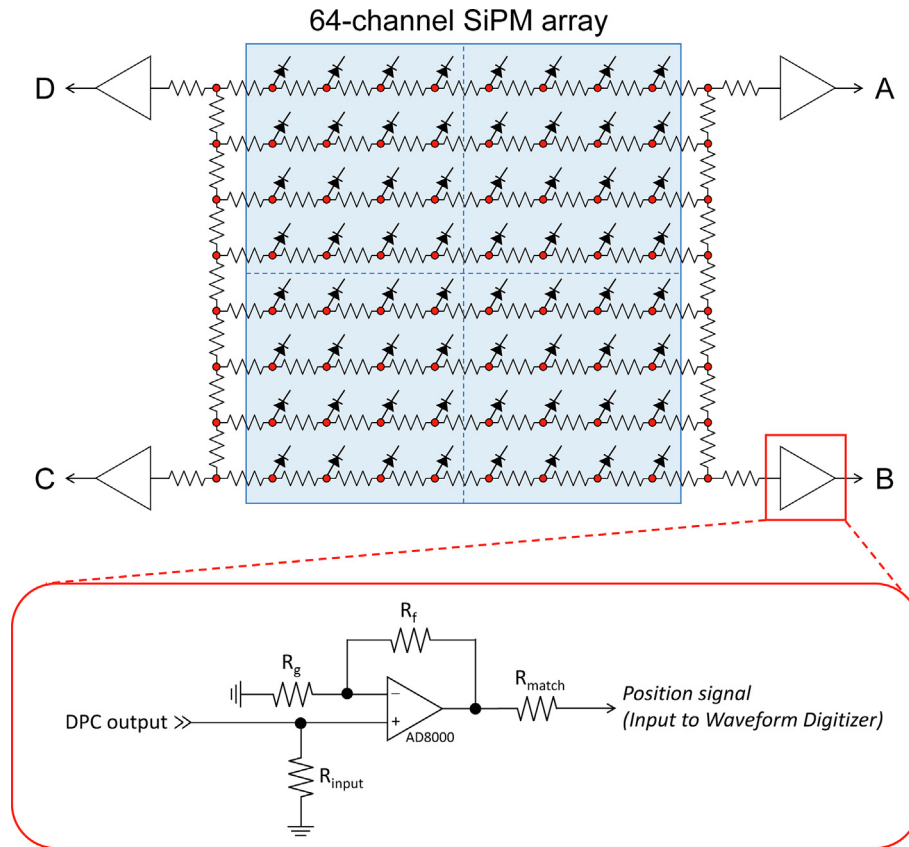


Fig. 2.  $8 \times 8$  charge division multiplexing circuit for position and energy information.

detector in a thermostatic chamber (20 °C). A low-activity (15  $\mu\text{Ci}$ )  $^{22}\text{Na}$  point source (MMS06-022; Eckert & Ziegler, Germany) was placed at the front panel of the reference detector to uniformly irradiate the PET detector module. The SiPMs mounted on the PET detector modules were operated at an optimal voltage of 58.0 V that corresponded to the overvoltage of approximately 4.0 V. The output signals of the PET detector module were fed into a domino-ring-sampler 4 (DRS4)-based high-speed waveform digitizer (DT5742B; CAEN, Italy) that exhibits a 5-GSPS sampling rate with a 12-bit sampling resolution. With respect to coincidence acquisition, a series of nuclear instrument modules (NIMs) were utilized [32]. The PMT dynode signal of the reference detector was replicated via a fan-in/fan-out module (N401; CAEN, Italy) and sequentially fed into a constant fraction discriminator module (N843; CAEN, Italy) to generate a *Reference trigger*. The *Module trigger* and *Reference trigger* were then connected to an AND logic gate (N455; CAEN, Italy) to generate a *Coincidence trigger* as an input to the DRS4-based high-speed waveform digitizer.

#### 2.4. Data analysis

The energy deposited in the PET detector module was estimated by determining the charge of *Position signals* (i.e.  $Q_A$ ,  $Q_B$ ,  $Q_C$ , and  $Q_D$ ) during an interval of 150 ns. The energy resolution was calculated by fitting the 511-keV photopeak on the energy histogram by using a Gaussian function. A 2D flood histogram was generated using the coincidence events within the energy window ranging from 250 keV to 750 keV. The interacted position of gamma photons in the 2D flood histogram, namely  $x$  and  $y$ , was decoded by using the energy information of each *Position signal* based on the following equations, respectively.

$$x = \frac{Q_A + Q_B - Q_C - Q_D}{Q_A + Q_B + Q_C + Q_D}$$

$$y = \frac{Q_A - Q_B - Q_C + Q_D}{Q_A + Q_B + Q_C + Q_D}$$

The arrival time of gamma photons was determined from each *Timing signal*. The recorded *Timing signals* were 10-fold oversampled based on the spline interpolation method to decrease the effect of the quantization error. Subsequently, the arrival timestamps were generated by using the oversampled *Timing signals* based on the digital leading-edge discriminator (LED) method with varying thresholds from 10 mV to 50 mV after event-by-event baseline correction. In the coincidence resolving time (CRT) measurement, only the coincidence events within a 20% window around the 511-keV photopeak were taken into account. Here, we used 2,000,000 coincidence events for the CRT analysis. The CRT was then estimated as a FWHM value of the time-difference histogram fitted on a Gaussian function. The CRT between the PET detector modules ( $\text{CRT}_{\text{DET/DET}}$ ) was estimated via quadratically subtracting the known STR value of the reference detector from the CRT value between the PET detector module and reference detector and multiplying the result with  $\sqrt{2}$  [33]. We repeated the experiments with three different multiplexing ratios corresponding to 16:1, 32:1, and 64:1. Energy resolution and CRT values were reported for upper and lower crystal-layers on a per-crystal basis.

### 3. Results and discussion

All LSO crystals in both the upper and lower crystal-layers were clearly identified in the 2D flood histogram, even at the edge and corner of the crystal arrays (Fig. 5(a)), and yielded good energy resolutions corresponding to  $10.5 \pm 1.0\%$  (upper) and  $12.1 \pm 1.6\%$  (lower), respectively (Fig. 5(b)). No remarkable differences in the 2D flood histogram and energy resolution were observed among the outcomes of three different timing multiplexing ratios corresponding to 16:1, 32:1, and 64:1.

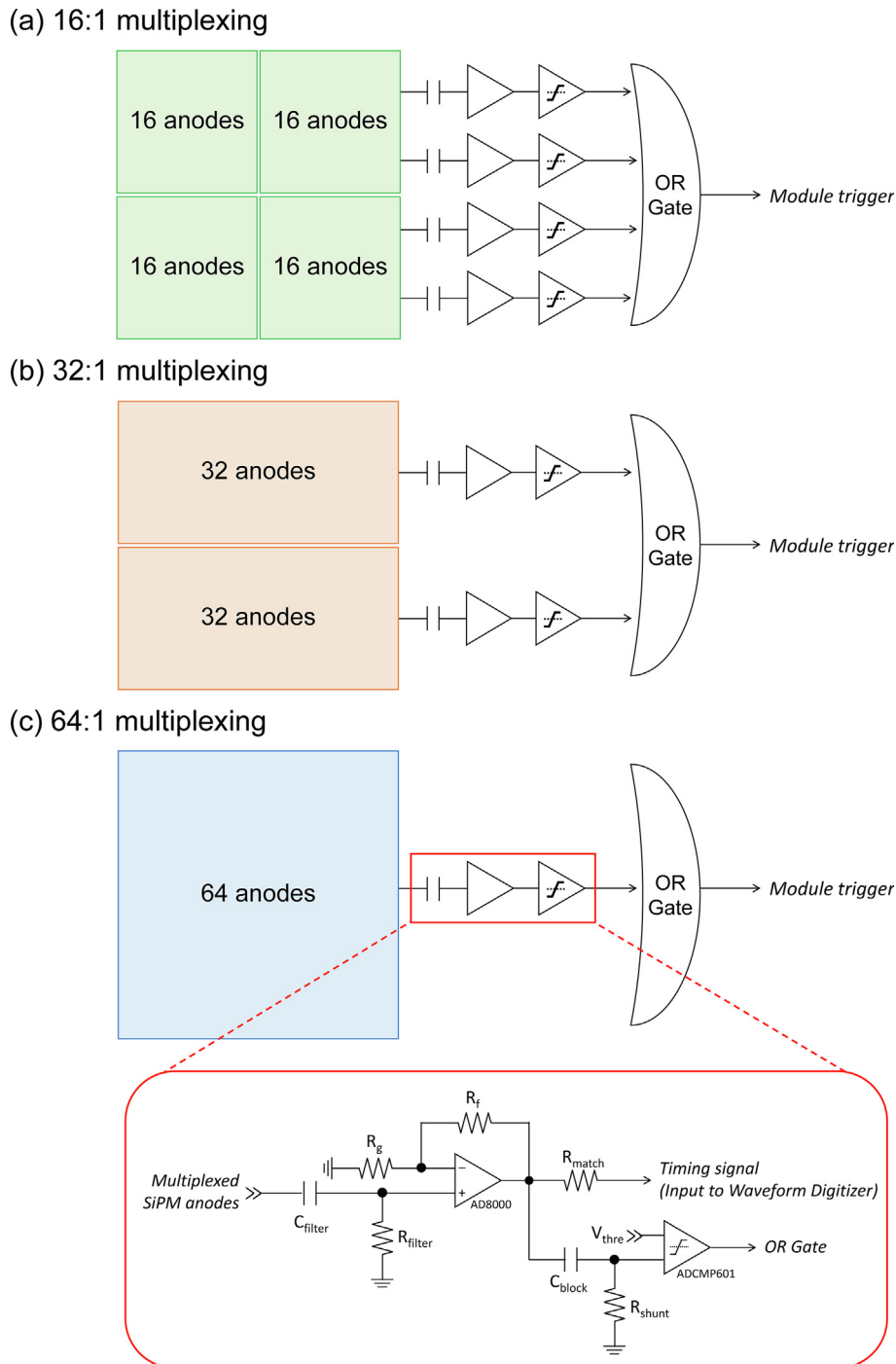


Fig. 3. Multiplexing circuit of 64 SiPM anodes for timing information; (a) 16:1 multiplexing, (b) 32:1 multiplexing, and (c) 64:1 multiplexing.

Fig. 6 shows the  $CRT_{DET/DET}$  value as a function of LED threshold for each 16:1, 32:1, and 64:1 multiplexing readout of *Timing signals*. The optimal timing performance was observed in 16:1 multiplexing and exhibited the lowest CRT values corresponding to  $325 \pm 39$  ps FWHM for upper crystal-layer and  $342 \pm 55$  ps FWHM for lower crystal-layer. Interestingly, no significant degradation in the timing performance was observed with increases in the multiplexing ratio and yielded CRT values corresponding to  $330 \pm 37$  ps FWHM (upper) and  $345 \pm 48$  ps FWHM (lower) for 32:1 multiplexing and  $336 \pm 22$  ps FWHM (upper) and  $347 \pm 32$  ps FWHM (lower) for 64:1 multiplexing, respectively. The experimental results demonstrated that the first-order high-pass filtering of SiPM signals effectively mitigated the CRT degradation in large-area SiPM arrays and maintained good timing performance even

for the 64:1 multiplexing readout scheme. Slight degradation of the timing performance in the 64:1 multiplexing would be attributed to the accumulated resistance-capacitance (RC) constant.

An interesting feature in per-crystal CRT maps is worth noting. As shown in Fig. 7, the 16:1 and 32:1 multiplexing readout schemes exhibit CRT degradation along the boundaries of monolithic 16-channel SiPMs (i.e. the red-dotted line in Fig. 7) while the 64:1 multiplexing does not exhibit this type of CRT degradation. This is because the amplitude of 16:1- or 32:1-multiplexed *Timing signal* generated at the boundaries was relatively low due to light dispersion to other *Timing signals*, thereby increasing the uncertainty in time pick-off based on the LED method.

With respect to the aspect of circuit implementation, the front-end

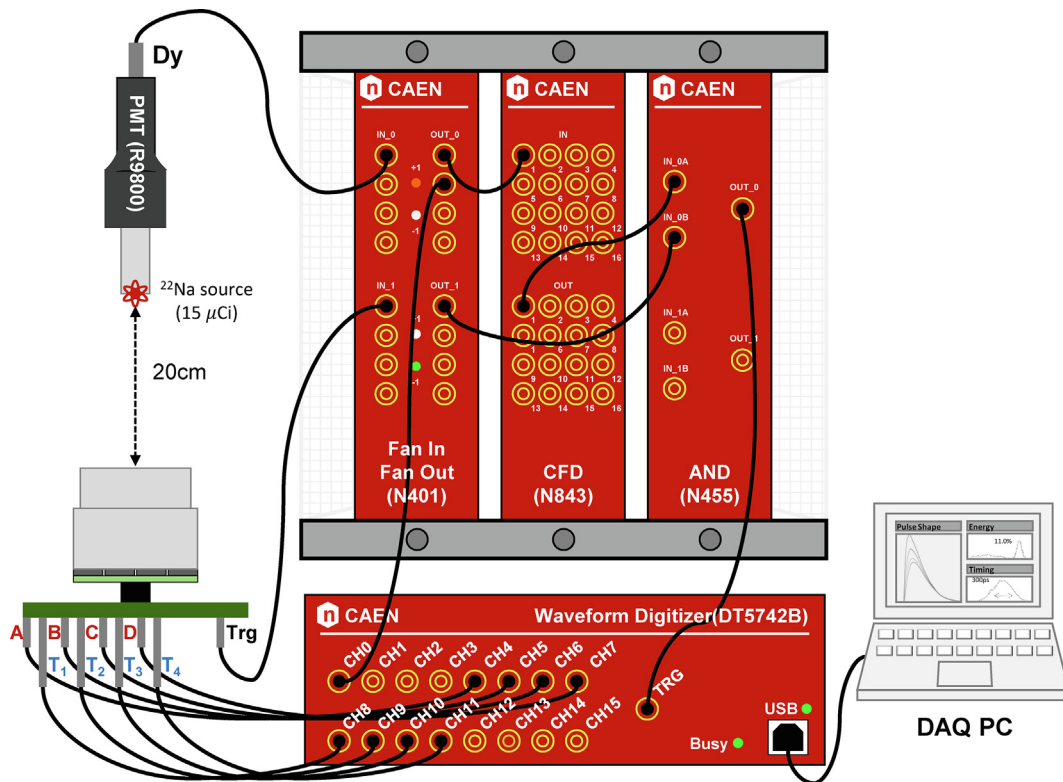


Fig. 4. Experimental setup used in this study. (Dy: PMT dynode signal; A,B,C,D: Position signals; T<sub>1</sub>,T<sub>2</sub>,T<sub>3</sub>,T<sub>4</sub>: Timing signals; Trg: Module trigger).

electronics design with 64:1 multiplexing is also simpler than that of 16:1 and 32:1 multiplexing readout schemes because the 64:1 multiplexing requires only an LVCMOS comparator and the absence of a digital OR logic gate to generate the *Module trigger*. However, the effects of the signal multiplexing on the timing and count-rate performance of PET system should be further investigated.

We demonstrated the feasibility of the 64:1 multiplexing readout via the high-resolution PET detector module with TOF and DOI capabilities. To further take the advantage of the 64:1 multiplexing readout scheme, it is worth considering to utilize a common-cathode readout of the SiPM arrays. The multiplexing readout investigated in this study was based on SiPM anodes and therefore requires at least 64 resistors. On the other hand, the common-cathode readout only requires a single capacitor as an input to the high-gain amplifier to obtain *Timing signals*, and this further decreases the number of electronic components in the PCB design. However, the common-cathode approach might lead to the undershoot of *Position signals*. Therefore, when using the common-cathode readout scheme, it is necessary to carefully perform the charge collection of *Position signals* to avoid the degradation of energy resolution and 2D flood histogram quality.

The aforementioned results indicate that the highly multiplexed SiPM signal readout for the timing channel can be a practical solution to decrease the readout burden of the DAQ system with only a slight degradation in the PET timing performance. However, there is more room for improvement in CRT without replacing photosensors or crystal blocks. Several studies demonstrated the improvement in CRT via the application of the time-walk correction of LED method [34,35]. The TOF capability of the PET detector module could be further enhanced via embedding firmware that achieves on-the-fly calibration of LED time-walk in the subsequent DAQ system, thereby achieving < 300 ps CRT.

With respect to system implementation, the proposed concept can be applied to construct a full-ring brain-dedicated PET system in a compact manner. This is because our proposed PET detector module integrated with the highly multiplexed SiPM readout scheme provides a scalable solution by extending the detector modules along with transverse and axial directions via high-density connectors. Although our investigation was being focused on the development of brain-dedicated PET scanners, the proposed concept also can be utilized to construct other high-resolution organ-dedicated PET scanners [36] without the

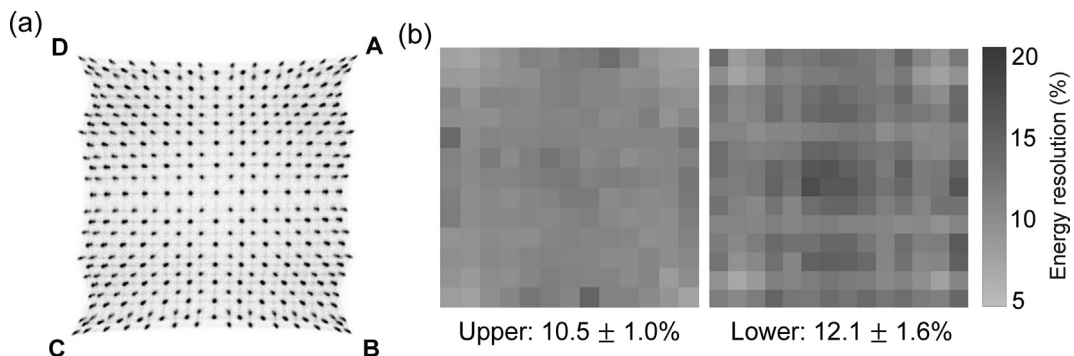


Fig. 5. (a) 2D flood histogram, (b) Per-crystal energy resolution map obtained from the PET detector module.

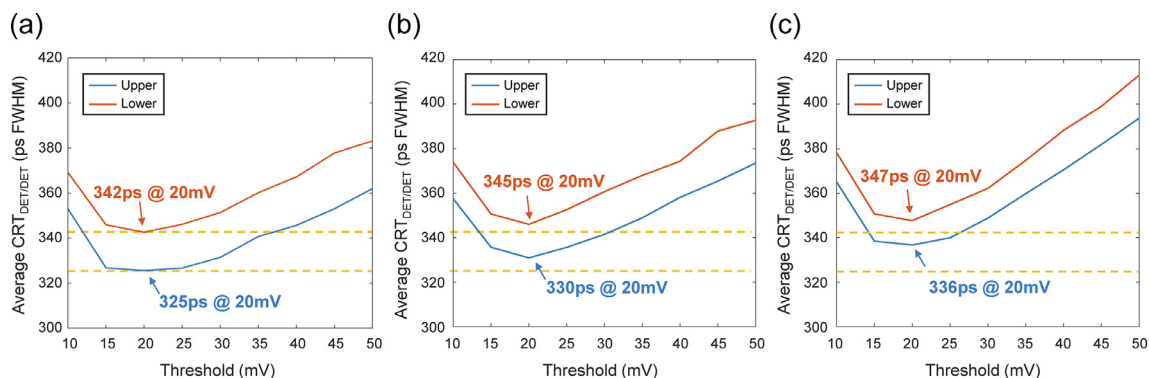


Fig. 6. Average CRT values of the PET detector module as a function of LED threshold for each (a) 16:1 multiplexing, (b) 32:1 multiplexing, and (c) 64:1 multiplexing readout scheme.

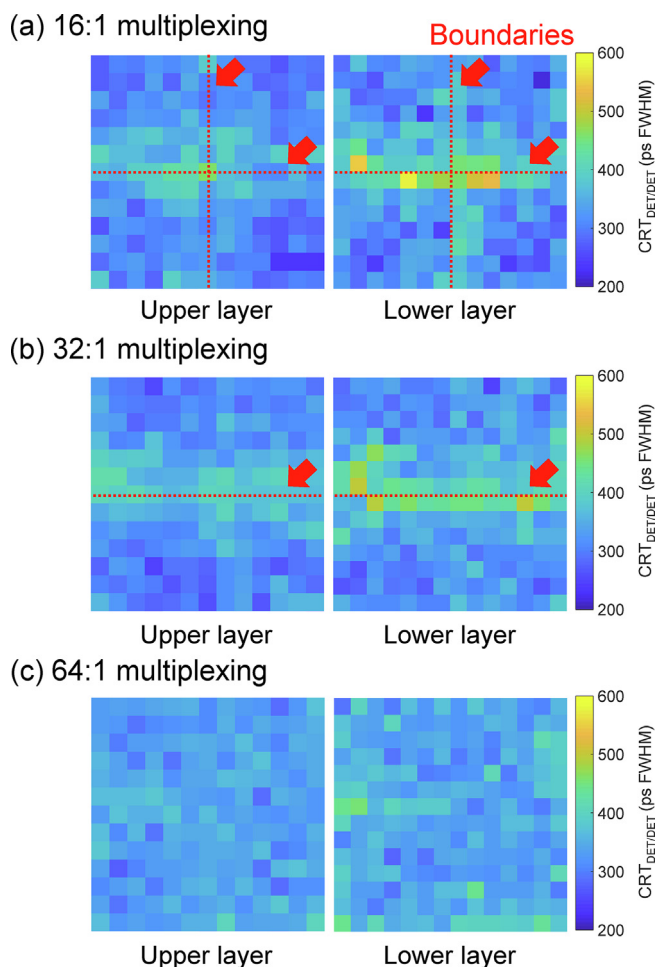


Fig. 7. Per-crystal CRT map at 20 mV LED threshold for each (a) 16:1, (b) 32:1, and (c) 64:1 multiplexing readout scheme. Red-dotted line denotes the boundary of monolithic 16-channel SiPMs for each of the 16:1, 32:1, and 64:1 multiplexing readout schemes. (For interpretation of the references to colour in this figure legend, the reader is referred to the web version of this article.)

requirement of a large number of DAQ channels. Our next milestone is to build a full-ring brain-dedicated PET system by utilizing the high-resolution PET detector modules investigated in this study.

#### 4. Conclusions

In this study, we investigated the characteristics of the highly multiplexed readout of SiPM signals via the PET detector module with

the two-layer relative-offset DOI crystal block and 64-channel large-area SiPM array. In particular, the timing performance of the PET detector module was only slightly compromised with the 64:1 multiplexing relative to the 16:1 multiplexing, thereby demonstrating that the first-order high-pass filter could be a simple and practical solution that avoids severe timing degradation in developing the brain-dedicated PET scanners with TOF and DOI capabilities.

#### Acknowledgments

This work was supported by grants from National Research Foundation of Korea (NRF) funded by Korean Ministry of Science, ICT and Future Planning (grant no. NRF-2016R1A2B3014645) and Korea Health Technology R&D Project through Korea Health Industry Development Institute (KHIDI) funded by Korean Ministry of Health and Welfare (South Korea) (grant no. HI14C1135).

#### References

- [1] Jung JH, Choi Y, Jung J, Kim S, Lim HK, Im KC, et al. Development of PET/MRI with insertable PET for simultaneous PET and MR imaging of human brain. *Med Phys* 2015;42:2354–63.
- [2] Gong K, Majewski S, Kinahan PE, Harrison RL, Elston BF, Manjeshwar R, et al. Designing a compact high performance brain PET scanner-simulation study. *Phys Med Biol* 2016;61:3681–97.
- [3] González AJ, González-Montoro A, Vidal LF, Barbera J, Aussenhofer S, Hernandez L, et al. Initial results of the MINDView PET insert inside the 3T mMR. *IEEE Trans Rad Plasma Med Sci* 2018;3:343–51.
- [4] Tashima H, Yamaya T. Proposed helmet PET geometries with add-on detectors for high sensitivity brain imaging. *Phys Med Biol* 2016;61:7205–20.
- [5] Kapusta M, Mintzer R, Byars L, Catana C, Schmand M. High spatial resolution time of flight PET detectors for brain imaging. *IEEE NSS MIC Conf Proc* 2017:1–6.
- [6] Watanabe M, Saito A, Isobe T, Ote K, Yamada R, Moriya T, et al. Performance evaluation of a high-resolution brain PET scanner using four-layer MPPC DOI detectors. *Phys Med Biol* 2017;62:7148–66.
- [7] Belcarì N, Bisogni MG, Camarlinghi N, Carra P, Cerello P, Morrocchi M, et al. Design and detector performance of the PET component of the TRIMAGE PET/MR/EEG scanner. *IEEE Trans Rad Plasma Med Sci* 2019;3:292–301.
- [8] Lv Y, Lv X, Liu W, Judenhofer MS, Zwingerberger A, Mini Wisner E, et al. a prototype high-sensitivity PET/CT scanner for companion animal whole body and human brain scanning. *Phys Med Biol* 2019;64:075004.
- [9] Yamaya T, Hagiwara N, Obi T, Tsuda T, Kitamura K, Hasegawa T, et al. Preliminary resolution performance of the prototype system for a 4-layer DOI-PET scanner: jPET-D4. *IEEE Trans Nucl Sci* 2006;53:1123–8.
- [10] Spanoudaki VC, Levin CS. Investigating the temporal resolution limits of scintillation detection from pixelated elements: comparison between experiment and simulation. *Phys Med Biol* 2011;56:735–56.
- [11] Yu Y, Wang S, Wang X, Xia Y, Shang H, Wu J, et al. Impact of depth-of-interaction on image resolution in long axial-POV. *IEEE NSS MIC Conf Proc* 2014:10–3.
- [12] Zhang N, Thompson CJ, Togane D, Cayouette F, Nguyen KQ. Anode position and last dynode timing circuits for dual-layer BGO scintillator with PS-PMT based modular PET detectors. *IEEE Trans Nucl Sci* 2002;49:2203–7.
- [13] Hong SJ, Kwon SI, Ito M, Lee GS, Sim KS, Park KS, et al. Concept verification of three-layer DOI detectors for animal PET. *IEEE Trans Nucl Sci* 2008;55:912–7.
- [14] Ito M, Lee JS, Kwon SI, Lee GS, Hong B, Lee KS, et al. A four-layer DOI detector with a relative offset for use in animal PET system. *IEEE Trans Nucl Sci* 2010;57:976–82.
- [15] Miller M, Zhang J, Binzel K, Griesmer J, Laurence T, Narayanan M, et al. Characterization of the Vereos digital photon counting PET system. *J Nucl Med*

- 2015;56(Suppl 3):434.
- [16] Levin CS, Maramraju SH, Khalighi MM, Deller TW, Delso G, Jansen F. Design features and mutual compatibility studies of the time-of-flight PET capable GE SIGNA PET/MR system. *IEEE Trans Med Imaging* 2016;35:1907–14.
- [17] van Sluis JJ, de Jong J, Schaar J, Noordzij W, van Snick P, Dierckx R, et al. Performance characteristics of the digital Biograph Vision PET/CT system. *J Nucl Med* 2019;60:1031–6.
- [18] Hegazy MA, Cho MH, Cho MH, Lee SY. U-net based metal segmentation on projection domain for metal artifact reduction in dental CT. *Biomed Eng Lett* 2019;9:375–85.
- [19] Mansour RF. Deep-learning-based automatic computer-aided diagnosis system for diabetic retinopathy. *Biomed Eng Lett* 2018;8:47–57.
- [20] Kang SK, Seo S, Shin SA, Byun MS, Lee DY, Kim YK, et al. Adaptive template generation for amyloid PET using a deep learning approach. *Hum Brain Mapp* 2018;39:3769–78.
- [21] Park J, Bae S, Seo S, Park S, Bang J-I, Han JH, et al. Measurement of glomerular filtration rate using quantitative SPECT/CT and deep-learning-based kidney segmentation. *Sci Rep* 2019;9:4223.
- [22] Hwang D, Kim KY, Kang SK, Seo S, Paeng JC, Lee DS, et al. Improving accuracy of simultaneously reconstructed activity and attenuation maps using deep learning. *J Nucl Med* 2018;59:1624–9.
- [23] Hwang D, Kang SK, Kim KY, Seo S, Paeng JC, Lee DS, et al. Generation of PET attenuation map for whole-body time-of-flight 18F-FDG PET/MRI using a deep neural network trained with simultaneously reconstructed activity and attenuation maps. *J Nucl Med* 2019;60:1183–9.
- [24] Liu C-Y, Goertzen AL. Multiplexing approaches for a  $12 \times 4$  array of silicon photomultipliers. *IEEE Trans Nucl Sci* 2014;61:35–43.
- [25] Cates JW, Bieniosek MF, Levin CS. Highly multiplexed signal readout for a time-of-flight positron emission tomography detector based on silicon photomultipliers. *J Med Imaging* 2017;4:011012.
- [26] Kim H, Hua Y, Lyu X, Xu F, Wang Y, Lyu J, et al. A systematic study on the strip-line readout method for SiPM-based TOF PET. *IEEE NSS MIC Conf Proc* 2017:1–3.
- [27] Nakazawa M, Tsuda T, Furumiya T, Adachi S, Ohi J, Kitamura K. Development of a 64ch SiPM-based TOF-PET detector with high spatial and timing resolutions using multiplexing architecture. *IEEE NSS MIC Conf Proc* 2017:1–3.
- [28] Ko GB, Lee JS. Single transmission-line readout method for silicon photomultiplier based time-of-flight and depth-of-interaction PET. *Phys Med Biol* 2017;62:2194–207.
- [29] Bieniosek MF, Cates JW, Levin CS. Achieving fast timing performance with multiplexed SiPMs. *Phys Med Biol* 2016;61:2879–92.
- [30] Bieniosek MF, Cates JW, Grant AM, Levin CS. Analog filtering methods improve leading edge timing performance of multiplexed SiPMs. *Phys Med Biol* 2016;61:N427–40.
- [31] Siegel S, Silverman RW, Shao Y, Cherry SR. Simple charge division readouts for imaging scintillator arrays using a multi-channel PMT. *IEEE Trans Nucl Sci* 1996;43:1634–41.
- [32] Park H, Lee S, Ko GB, Lee JS. Achieving reliable coincidence resolving time measurement of PET detectors using multichannel waveform digitizer based on DRS4 chip. *Phys Med Biol* 2018;63:24NT02.
- [33] Park H, Ko GB, Lee JS. Hybrid charge division multiplexing method for silicon photomultiplier based PET detectors. *Phys Med Biol* 2017;62:4390–405.
- [34] Gola A, Piemonte C, Tarolli A. The DLED algorithm for timing measurements on large area SiPMs coupled to scintillators. *IEEE Trans Nucl Sci* 2012;59:358–65.
- [35] Du J, Schmall JP, Judenhofer MS, Di K, Yang Y, Cherry SR. A time-walk correction method for PET detectors based on leading edge discriminators. *IEEE Trans Rad Plasma Med Sci* 2017;1:385–90.
- [36] González AJ, Sánchez F, Benlloch JM. Organ-dedicated molecular imaging systems. *IEEE Trans Rad Plasma Med Sci* 2018;2:388–403.